communications physics

ARTICLE

https://doi.org/10.1038/s42005-023-01326-6 OPEN

Realization of Wilson fermions in topolectrical circuits

Huanhuan Yang [1], Lingling Song[1], Yunshan Cao[1] & Peng Yan [1✉]

The Wilson fermion (WF) is a fundamental particle in the theory of quantum chromodynamics. Theoretical calculations have shown that the WF with a half skyrmion profile represents a quantum anomalous semimetal phase supporting a chiral edge current, but the experimental evidence is still lacking. In this work, we report a direct observation of the WF in circuit systems. We find that WFs manifest as topological spin textures analogous to the half skyrmion, half-skyrmion pair, and Néel skyrmion structures, depending on their mass. Transformations of different WF states are realized by tuning the electric elements. We further experimentally observe the propagation of chiral edge current along the domain-wall separating two circuits with contrast fractional Chern numbers. Our work provides experimental evidence for WFs in topolectrical circuits. The nontrivial analogy between the WF state and the skyrmionic structure builds an intimate connection between the two burgeoning fields.

[1] School of Physics and State Key Laboratory of Electronic Thin Films and Integrated Devices, University of Electronic Science and Technology of China, Chengdu 610054, China. ✉email: yan@uestc.edu.cn

Lattice quantum chromodynamics is an effective method to study the strong interactions of quarks mediated by gluons[1,2]. In lattice quantum chromodynamics calculation, quarks are represented by fermionic fields and placed at lattice sites, and gluons play the role of interactions between neighboring sites[3]. However, when naively putting the fermionic fields on a lattice, we will meet the fermion doubling problem[4], i.e., the emergence of 2^d-1 spurious fermionic particles for each original fermion (d is the dimension of the spacetime). The origin of the doubling problem is deeply connected with chiral symmetry and can be traced back to the axial anomaly[5]. To remove the ambiguity, Kenneth Wilson developed a technique by introducing wave-vector-dependent mass, which modifies the Dirac fermions to Wilson ones[6]. The fermion doubling issue exists in condensed matter physics as well[7–11]. It prevents the occurrence of quantum anomalies in lattices, such as the quantum anomalous Hall insulator[10] and Weyl semimetal with single node[11]. It is known that Dirac fermions manifest as the low-energy excitations of topological semimetals/insulators (e.g., graphene)[12–15]. However, the observation of Wilson fermion (WF) is yet to be realized.

Recent works show that electrical circuits can be used to mimic and explore the properties of both bosons[16,17] and fermions[18–20]. In this work, we utilize a lattice model to realize the WF and probe it in topolectrical circuit experiments[20–39]. We find that the nontrivial state of the WF strongly depends on its mass and can be classified into three categories characterized by different Chern numbers of 0, ±1/2, and ±1, corresponding to the half-skyrmion pair, half skyrmion, and Néel skyrmion, respectively. We propose a circuit method to efficiently manipulate the transport and transformation of the WF states. In this system, the fractional Chern number dictates a quantum anomalous semimetal (QASM) phase with a chiral edge current as suggested in ref. [40]. Here, we report a direct observation of the chiral current along the domain wall (DW) separating two circuits with contrast fractional Chern numbers being 1/2 and −1/2. WFs in a three-dimensional (3D) circuit system are constructed as well. They are characterized by 3D winding numbers and accompanied by the emergence of the surface states and DW states at the boundaries. Our work opens the door for realizing the exotic WFs in solid-state systems.

Results and discussion

We begin from the Dirac Hamiltonian $\mathcal{H} = c\mathbf{k}\cdot\alpha + mc^2\beta$ with c the light speed, $\mathbf{k}$ the wave vector, and α, β being the Dirac matrices, which describes a Dirac fermion with the mass m[41]. Expressing this Dirac Hamiltonian on a lattice of the tight-binding form, we obtain $\mathcal{H}_{\mathrm{D}} = \sum_{i=1}^{d} \frac{\hbar v}{a}\sin(k_i a)\alpha_i + mv^2\beta$ with a the lattice constant and $\hbar v$ the hopping strength (d is the space dimension). It is straightforward to verify that $2^d - 1$ non-physics fermion doublers appear at the Brillouin zone (BZ) boundaries $k_i = \pi/a$. Following Wilson's method, we derive the WF Hamiltonian of the following form $\mathcal{H} = \mathcal{H}_{\mathrm{D}} + \mathcal{H}_{\mathrm{W}}$ with $\mathcal{H}_{\mathrm{W}} = \frac{4b}{a^2}\sin^2\frac{k_i a}{2}\beta$ being the $\mathbf{k}$-dependent Wilson mass term[40]. Here, the $\mathbf{k}$-independent mass m in Hamiltonian $\mathcal{H}_{\mathrm{D}}$ is referred to as the dispersionless mass of WFs. It is noted that the $\mathcal{H}_{\mathrm{W}}$ term breaks the parity symmetry in two-dimensional (2D) and chiral symmetry in 3D cases, which can circumvent the fermion doubling problems[4] and reproduce the quantum anomaly in the continuum limit. In Supplementary Note I, we show the details how the doublers from Dirac Hamiltonian are removed by introducing the Wilson mass term. Next, we report the realization of the Wilson Hamiltonian in electrical circuits.

Circuit model. We consider a 2D spinful square lattice in Fig. 1a. The circuit is constituted by four types of capacitors $\pm C_{1,2}$ and the negative impedance converters with current inversion (INICs) in Fig. 1b, where A and B parts correspond to the massless Dirac and Wilson mass Hamiltonians, respectively. It is noted that one can utilize inductors to replace negative capacitors because the admittance of the negative capacitor $-i\omega C$ is equivalent to the inductor $-i\frac{1}{\omega L}$ for $L = 1/(C\omega^2)$[42]. Here, ω is the working frequency. We implement two sites to imitate a (pseudo-) spin, indicated by the red rectangle in Fig. 1a, b. The INIC is set up by an operational amplifier and three identical resistors R, as shown in Fig. 1c. In Fig. 1d, we show the realization of the staggered on-site potential, which is modeled as the dispersionless mass of WF.

The circuit response is governed by Kirchhoff's law $I(\omega) = \mathcal{J}(\omega)V(\omega)$ with I the input current and V the node voltage. $\mathcal{J}(\omega, \mathbf{k})$ is the circuit Laplacian written as

$$\mathcal{J}(\omega, \mathbf{k}) = \begin{pmatrix} j_{11} & j_{12} \\ j_{21} & j_{22} \end{pmatrix}, \tag{1}$$

where $j_{11} = 4i\omega C_2 - 2i\omega C_2(\cos k_x + \cos k_y) + 4i\omega\Delta C_2, j_{12} = 2iG\sin k_x + 2\omega C_1 \sin k_y, j_{21} = 2iG\sin k_x - 2\omega C_1 \sin k_y,$ and $j_{22} = -4i\omega C_2 + 2i\omega C_2(\cos k_x + \cos k_y) - 4i\omega\Delta C_2,$ with $G = 1/R$ the conductance and Δ being the mass coefficient of WFs. In the presence of conductance, the time-reversal symmetry ($\mathcal{T}$) of the system is broken because of $\mathcal{J}(\omega, \mathbf{k})^* \neq -\mathcal{J}(\omega, -\mathbf{k})$[27].

By expressing $\mathcal{J}(\omega) = i\mathcal{H}(\omega)$ with the Dirac matrices, we obtain

$$\mathcal{H}(\omega) = 2G\sin k_x\alpha_x + 2\omega C_1 \sin k_y\alpha_y + 4\omega C_2\left(\sin^2\frac{k_x}{2} + \sin^2\frac{k_y}{2}\right)\beta + 4\omega\Delta C_2\beta, \tag{2}$$

where α_x, α_y and β represent the Pauli matrices σ_x, σ_y, and σ_z, respectively. It is noted that the above Hamiltonian fully simulates the lattice model of WFs. The first three terms in Eq. (2) represent the Hamiltonian of WF, and the last term is the dispersionless mass of WF. Meanwhile, by tuning the electric elements parameters G, C_1, and C_2, one can conveniently manipulate the shape of Wilson cones (similar to the Dirac cones).

In what follows, we analyze the topological properties of the lattice model.

Topological phase and phase transition. For a $\mathcal{T}$-broken 2D two-band system, one can evaluate the Chern number[43]

$$\mathcal{C} = -\frac{1}{2\pi}\int_{\mathrm{BZ}}\left(\frac{\partial A_y}{\partial k_x} - \frac{\partial A_x}{\partial k_y}\right)dk_x dk_y, \tag{3}$$

to judge its topological properties. Here $\mathbf{A}(\mathbf{k}) = i\langle u_{\mathbf{k}}|\nabla_{\mathbf{k}}|u_{\mathbf{k}}\rangle$ is the Berry connection with $|u_{\mathbf{k}}\rangle$ the eigenstate of lower band.

In following calculations, we adopt $C_i = C = 1$ nF ($i = 1, 2$), $f = \omega/(2\pi) = 806$ kHz (In experiments, we will use $L = 39\,\mu$H to replace $-C$, so we choose $\omega = 1/\sqrt{LC}$), and $G = \omega C = 0.005\,\Omega^{-1}$ ($R = 200\,\Omega$). Calculations of Chern number as a function of the dispersionless mass parameter Δ are plotted in Fig. 2a. We find the Chern numbers are quantized to five values ± 1, $\pm\frac{1}{2}$, and 0. It is noted that the Chern number is irrelevant to the value of C_1 but becomes opposite if C_2 changes its sign. We show the first BZ and typical band structures in Fig. 2b. Combined with the topological index, we classify these topological phases as follows. The band gaps open for the parameter intervals ① and ⑦, where the Chern number is zero. It gives the trivial insulator phase. For parameters in ② and ⑥, the band gaps close at M and Γ points, respectively. Surprisingly, the Chern numbers are quantized to $\mp 1/2$, respectively. This phase is dubbed the QASM[40]. For parameter zones ③ and ⑤, the band gaps open with the topological number $\mathcal{C} = \mp 1$, both of which represent Chern insulators with opposite

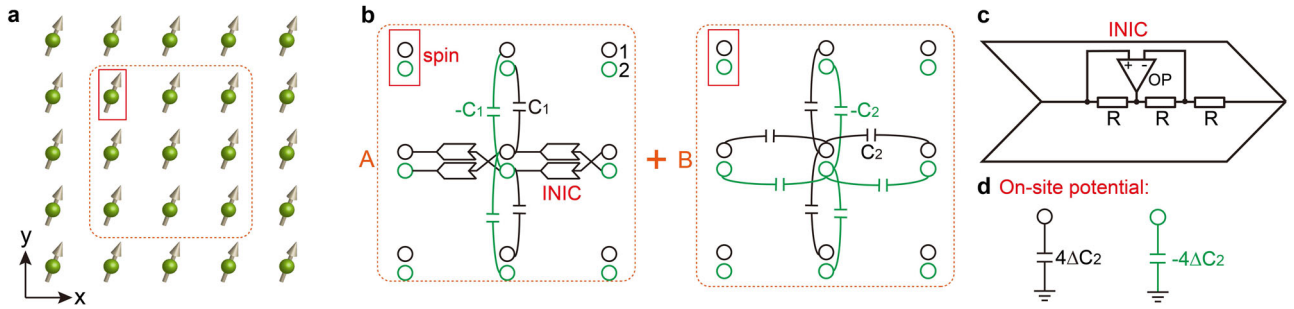

Fig. 1 Two-dimensional model of Wilson fermions. a Illustration of a 2D spinful square lattice. **b** The circuit realization of the hopping terms by A+B parts. Part A consists of two kinds of capacitors $\pm C_1$ and the negative impedance converters with current inversion (INICs). Part B is composed of two types of capacitors $\pm C_2$. The red rectangle indicates the correspondence between spin and circuit nodes. **c** Details of the INIC. The INIC is composed of an operational amplifier (OP) and three resistors R, acting as a positive (negative) resistor from right to left (left to right). **d** The realization of the staggered on-site potentials.

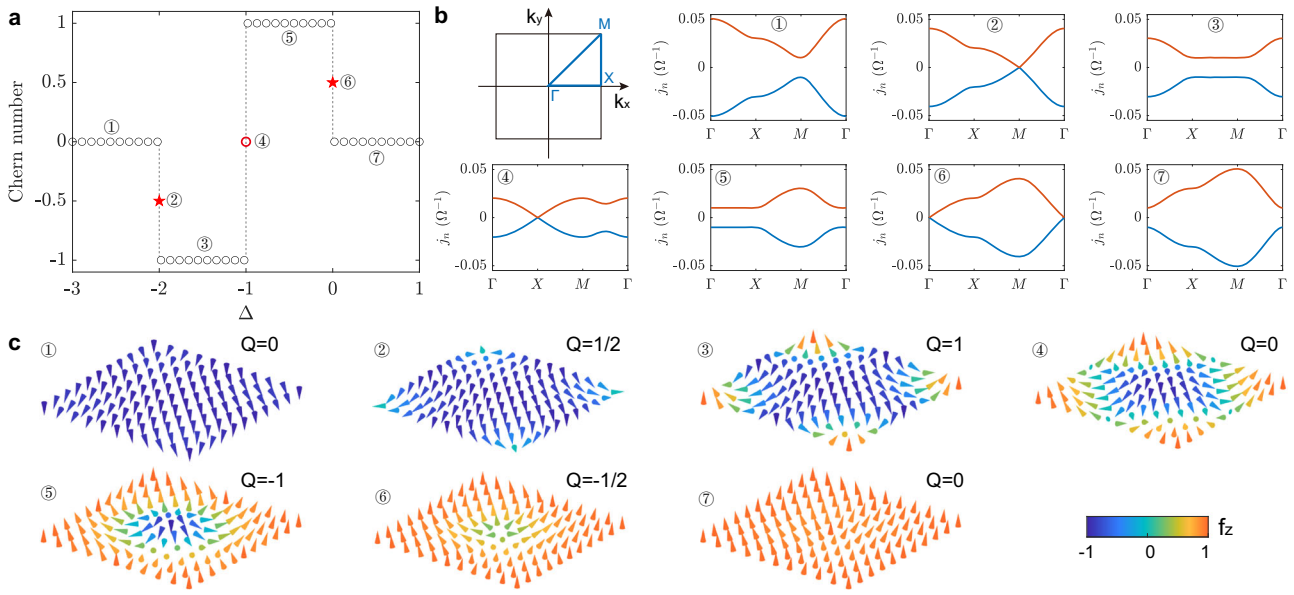

Fig. 2 Topological indexes and Wilson fermions. a The Chern number $\mathcal{C}$ steps as a function of the dispersionless mass Δ. The red stars and circle represent $\mathcal{C} = \pm\frac{1}{2}$ and $\mathcal{C} = 0$, corresponding to quantum anomalous semimetal and normal semimetal phases, respectively. **b** The first Brillouin zone and the typical band structures for $\Delta = -2.5, -2, -1.5, -1, -0.5, 0, 0.5$, respectively, corresponding to different parameter intervals in (**a**). The orange and blue curves indicate the two branches of band structures. **c** The spin textures of Wilson fermions in the momentum space.

chiralities. For the parameter region ④, the band structure closes at X point with a vanishing Chern number, indicating a normal semimetal phase.

By expressing Eq. (2) as $\mathcal{H} = \mathbf{f}(\mathbf{k}) \cdot \boldsymbol{\sigma}$, one can define a unit spin vector $\hat{\mathbf{f}}(\mathbf{k})$ as $\hat{\mathbf{f}}(\mathbf{k}) = \frac{\mathbf{f}(\mathbf{k})}{|\mathbf{f}(\mathbf{k})|}$, where $\mathbf{f}(\mathbf{k}) = (f_x, f_y, f_z)$ is the coefficient of Pauli matrices and $|\mathbf{f}(\mathbf{k})| = \sqrt{f_x^2 + f_y^2 + f_z^2}$. Figure 2c displays the spin textures of 2D WFs, which evolve as the increasing of dispersionless mass. The spin textures are reminiscent of the magnetic solitons in the condensed matter system[44–46]. It is observed that the spin textures of trivial insulator, Chern insulator, QASM, and normal semimetal correspond to the ferromagnetic ground state, skyrmion, half skyrmion, and half-skyrmion pair, respectively. By evaluating the topological charge $Q = \frac{1}{4\pi}\int_{\mathrm{BZ}} \hat{\mathbf{f}} \cdot (\frac{\partial \hat{\mathbf{f}}}{\partial k_x} \times \frac{\partial \hat{\mathbf{f}}}{\partial k_y}) dk_x dk_y$ in Fig. 2c, we identify an intimate connection with the Chern number as $Q + \mathcal{C} = 0$. This finding thus establishes an interesting map between WFs and magnetic solitons in electrical circuits.

In the broad spintronics community, the manipulation of skyrmion motion is crucial for the next-generation information industry[47]. Here, we propose a method to control the circuit skyrmion motion in momentum space. We first consider a skyrmion configuration with $\Delta = -0.5$. To generate a skyrmion propagation along k_x direction over a distance k_0, one can modify Eq. (2) to $\mathcal{H}(\omega) = 2G\sin(k_x - k_0)\sigma_x + 2\omega C_1 \sin k_y \sigma_y - 4\omega C_2 [\cos(k_x - k_0) + \cos k_y + \frac{1}{2}]\sigma_z$, which can be recast as $\mathcal{H}(\omega) = 2G' \sin k_x \sigma_x - 2G'' \cos k_x \sigma_x + 2\omega C_1 \sin k_y \sigma_y - [4\omega C_2' \cos k_x + 4\omega C_2'' \sin k_x + 4\omega C_2(\cos k_y + \frac{1}{2})]\sigma_z$. Compared with the original Eq. (2), one merely needs to modify two hopping strengths ($G' = G\cos k_0$ and $C_2' = C_2 \cos k_0$) and to add two extra hopping terms ($-2G'' \cos k_x \sigma_x$ and $4\omega C_2'' \sin k_x \sigma_z$). Variable resistors and capacitors can be conveniently adopted to realize these operations in circuit systems.

Quantum anomalous semimetals. To show the properties of QASM ($\Delta = 0$ with $\mathcal{C} = \frac{1}{2}$), we consider a ribbon configuration with periodic boundary condition along $\hat{x}$ direction and $N_y = 50$ nodes along $\hat{y}$ direction. Figure 3a shows the admittance spectra, where the conduction and valence bands touch at $k_x = 0$. There is

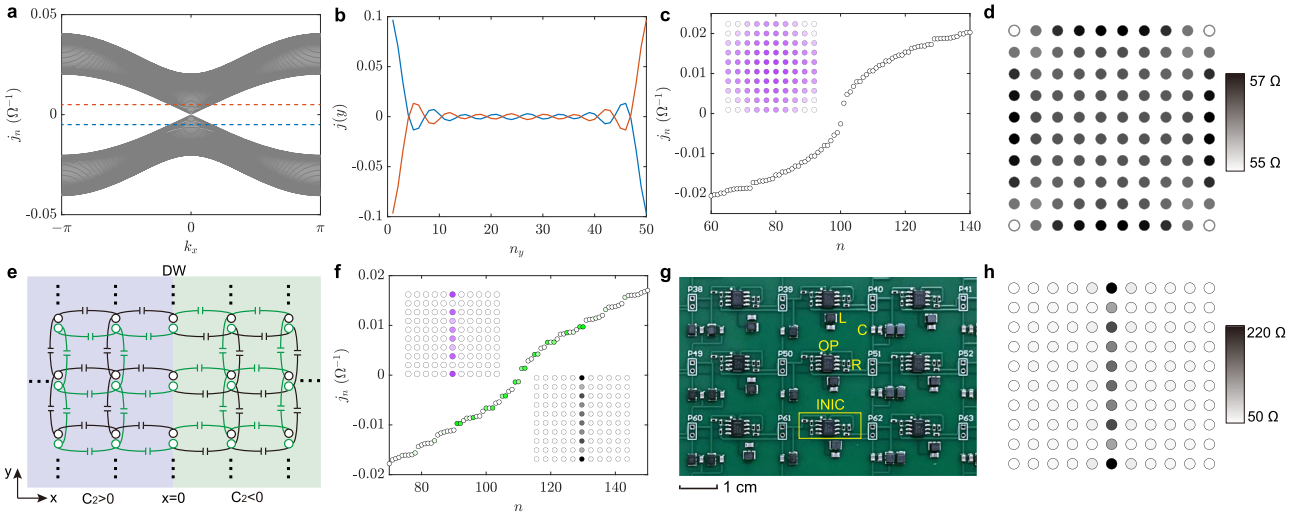

Fig. 3 Features of the quantum anomalous semimetal. a Admittance spectrum of the ribbon geometry. **b** The current density distribution for two different "Fermi" levels slightly deviating from the admittance eigenvalue $j_n = 0\,\Omega^{-1}$ (dashed lines in (**a**). **c** The admittance spectrum with the inset showing the wave functions near $j_n = 0\,\Omega^{-1}$. **d** The impedance distribution of the sample. **e** The configuration of the circuit domain wall with ± 1/2 topological charges in light blue and green regions. **f** The admittance spectrum. Insets: The distribution of the wave functions and impedances. **g** The partial printed circuit board used in the experiment. **h** Experimentally measured impedance.

no isolated band in this admittance spectra, so the edge state is absent. Considering the Hamiltonian (2), one can define a velocity operator as $v = 1/(i\hbar)[x, \mathcal{H}] = \frac{\partial \mathcal{H}}{\partial k_x} = 2G\cos k_x \sigma_x + 2\omega C_2 \sin k_x \sigma_z$. The transverse current density then can be written as

$$j(y) = \sum_n^{\varepsilon_n<\mu} \int [2G\cos k_x \phi_n^\dagger(k_x, y)\sigma_x \phi_n(k_x, y) + 2\omega C_2 \sin k_x \phi_n^\dagger(k_x, y)\sigma_z \phi_n(k_x, y)] dk_x, \tag{4}$$

with $\phi_n(k_x, y)$ being the wave functions of the n-th band and the sum index n indicating the bands below the admittance μ. We plot the current density for different positions in Fig. 3b. It is found that the current density decays from the boundary nodes, and its values are opposite for the top and bottom edges. Consequently, the chiral edge currents constitute the bulk-edge correspondence of QASM[40,48]. It is noted that the chiral current differs from the one in magnetic systems that originates from the chiral spin pumping effect induced by the topological structures in real space[49,50].

Then, we consider a 10×10 square lattice to study the finite-size effect. Diagonalizing the corresponding circuit Laplacian, we obtain the admittance spectra shown in Fig. 3c and the wave functions near $j_n = 0\,\Omega^{-1}$ in the inset of Fig. 3c. In our circuit, the impedance between the node a and the ground is computed by $Z_{a,\text{ground}} = \sum_n \frac{|\phi_{n,a}|^2}{j_n}$ with $\phi_{n,a}$ the wave function of node a for nth admittance mode, which reflects the features of wave functions near $j_n = 0\,\Omega^{-1}$ and can be measured readily[25,33]. By comparing Fig. 3d and 3c (inset), we find that the impedance of each node against the ground exhibits almost the same spatial distribution to wave functions, and one does not find an edge state.

To demonstrate the bulk-boundary correspondence, we consider a one-dimensional DW with 10×11 "spins" (an extra column is set up for DW configuration), as shown in Fig. 3e, where the capacitor C_2 has a kink at the center of the sample, i.e., $C_2 > 0$ (< 0) in the light blue (green) region. In this circumstance, the Chern number varies from 1/2 (left) to −1/2 (right). The eigenvalue and wave function of the bound state can be solved as $J = 2\omega C_1 k_y$ and $\phi(x, y) = \frac{1}{\sqrt{2\pi}}\chi_y \sqrt{\lambda}\exp(-\lambda|x| + ik_y y)$ with $\chi_y = \frac{\sqrt{2}}{2}(-i, 1)^{\mathrm{T}}$ and $\lambda = \frac{C_1}{|C_2|} + \sqrt{(\frac{C_1}{C_2})^2 + k_y^2}$. The nonzero eigenvalue means the bound states do not localize at zero admittance. One can obtain the effective velocity of the bound state $v_{\text{eff}} = \frac{\partial J}{\partial k_y} = 2\omega C_1$, indicting the DW bound state propagating along $\hat{y}$ direction (see Supplementary Note 2). In Fig. 3f, we show the admittance spectrum with the insets displaying the wave functions and impedances, from which one can clearly see the bound state confined inside the DW. Here, we use the inverse participation ratio $p = \lg(\sum_i |\phi_{n,i}|^4)$ of the system to characterize the localization properties of the wave functions[51,52], and the green dots indicate the localized state.

Then, we prepare a printed circuit board to verify the numerical results, as shown in Fig. 3g (see Methods for details). Figure 3h shows the experimental impedance distribution. It demonstrates a localized state between two domains, which compares well with the theoretical result in Fig. 3f. The existence of one bound state is closely related to the fact that the topological invariants between the two sides of the DW differ by 1. In addition, one cannot observe the edge states on the rest boundaries of the sample, which confirms that there is indeed no edge state. We also study the influence of the homogeneity of the circuit components on our results, which does not change our conclusion.

To show the chiral propagation of the bound state, we perform the circuit simulation with the software LTSPICE (http://www.linear.com/LTspice). By inputting a Gauss signal close to the DW, we observe the bound mode propagating along the $\hat{y}$ direction of DW. Finally, the voltage signal becomes a steady bound state inside the DW (see Supplementary Note 2).

Chern insulators and normal semimetal. To characterize Chern insulators ($\mathcal{C} = \pm 1$), we compute the admittance for a ribbon configuration, with the results being shown in Fig. S3 of Supplementary Note 3. For the parameter $\Delta = -0.5$ and -1.5, we find two crossing bands in the admittance gaps but with opposite charities. To show the chiral propagation of edge states, we perform the circuit simulation on a finite-size square lattice and observe a chiral voltage propagation (see Supplementary Note 3).

We note that at the phase transition point separating two Chern insulators ($\Delta = -1$), the Chern number vanishes but the spin texture is still non-trivial. We consider a finite-size lattice

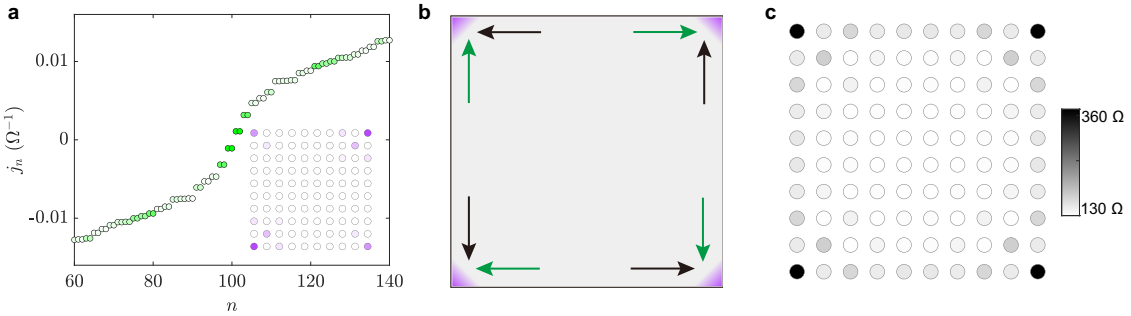

Fig. 4 The emergence of corner states. a The admittance of the finite-size square lattice with 10 × 10 "spins" with the inset showing the wave functions near the admittance eigenvalue $j_n = 0\,\Omega^{-1}$. **b** The corner state formed by the convergence of Chern insulators with opposite chiralities. **c** Numerical impedance.

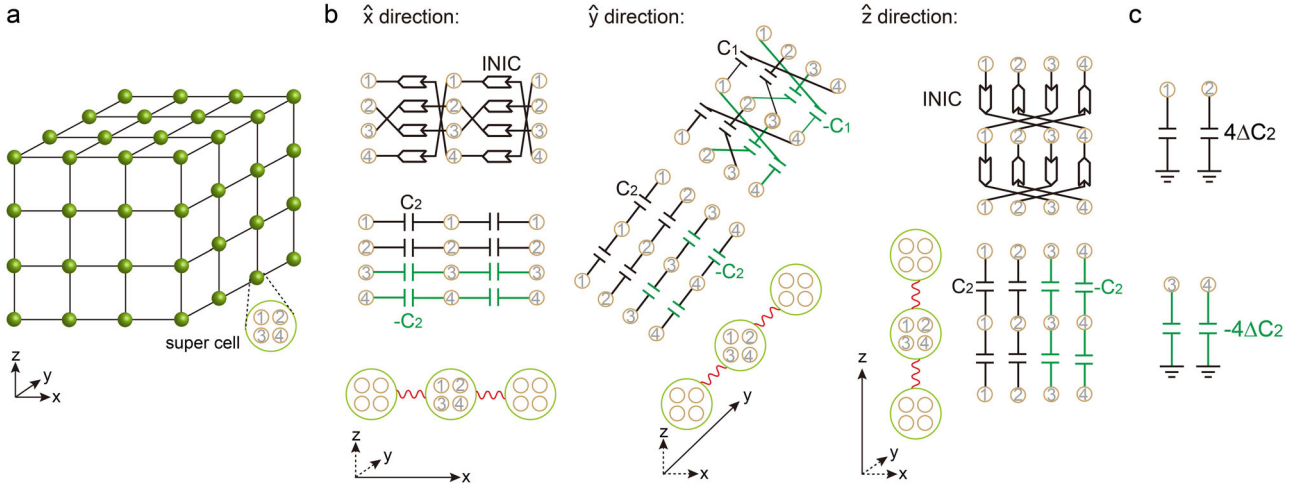

Fig. 5 Three-dimensional circuit model of Wilson fermions. a Three-dimensional hyper-cubic lattice model with four sites in each supercell. **b** The interactions between two cells along $\hat{x}$, $\hat{y}$, and $\hat{z}$ directions. **c** The realization of the on-site potentials.

with 10 × 10 "spins". The admittance spectrum is plotted in Fig. 4a, showing that a series of localized states lie near $j_n = 0\,\Omega^{-1}$, and the corner states lying at nonzero admittance is caused by the open of band gap at phase-transition point (see Supplementary Note 4). The wave functions of localized states are displayed in the inset of Fig. 4a, from which we identify a corner state. The origin of the emerging corner states can be interpreted as the convergence of two Chern insulators with opposite chiralities, as shown by the green and black arrows in Fig. 4b. Due to the contrast of the chirality, the one-dimensional edge states can only accumulate at the sample corners, forming the zero-dimensional localized states, i.e., corner states. These corner states can be detected by measuring the distributions of impedance, as shown in Fig. 4c. If we consider circular samples with these parameters, the corner states will disappear for the circle with a large radius (smooth boundary) and the wave functions will concentrate on the convex right angle of the sample for a small circle (see Supplementary Note 5).

Three-dimensional Wilson fermions. As a nontrivial generalization, we consider a 3D hyper-cubic lattice with four sites in each cell, as shown in Fig. 5a. The hopping terms and on-site potentials are shown in Fig. 5b, c, respectively. One can write the circuit Laplacian as $\mathcal{J}(\omega) = i\mathcal{H}(\omega)$ with

$$\mathcal{H}(\omega) = 2G\sin k_x\alpha_x + 2\omega C_1 \sin k_y\alpha_y + 2G\sin k_z\alpha_z + 4\omega C_2\left[\sin^2\frac{k_x}{2} + \sin^2\frac{k_y}{2} + \sin^2\frac{k_z}{2}\right]\beta + 4\Delta\omega C_2\beta, \quad (5)$$

where $\alpha_x = \sigma_x \otimes \sigma_x$, $\alpha_y = \sigma_x \otimes \sigma_y$, $\alpha_z = \sigma_x \otimes \sigma_z$, and $\beta = \sigma_z \otimes \sigma_0$ are Dirac matrices (see Supplementary Note 6).

The topological properties of the 3D system can be characterized by the winding number w_3[53]. We find that the topological index w_3 can only take five quantized values, i.e., 0, $\pm\frac{1}{2}$, ± 1. For the topological insulator phase $w_3 = 1$, one can observe surface states. At the border of the two topological insulators with opposite winding numbers, we find the hinge states induced by the overlap of the surface states. For the QASM phase $w_3 = 1/2$, we observe the bounded surface state in a finite-size DW circuit along the $\hat{x}$ direction (see Supplementary Note 6).

Conclusions

To summarize, we experimentally observed WFs in circuit systems. In addition, we mapped WFs with different masses or configurations to magnetic solitons with different skyrmion charges, which will enable us to study the properties of skyrmions, half skyrmions, and half-skyrmion pairs in electrical circuit platforms. We showed that the nontrivial spin-texture of WFs in momentum space is fully characterized by Chern numbers and winding number in 2D and 3D systems, respectively. The chiral edge current associated with the QASM state dictated by a fractional Chern number was directly detected. Although we have measured the band structures of WFs and their topological boundary states, how to reveal the quasiparticle nature of WFs is still an open question. Our work presents the first circuit realization of WFs, which sets a paradigm for other platforms, such as

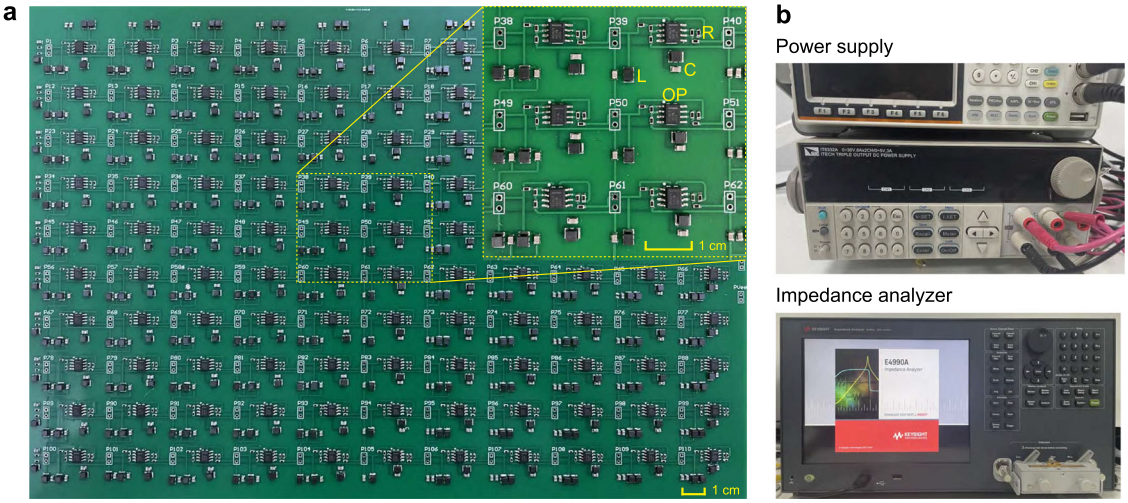

Fig. 6 Experimental layout. a The full image of the experimental printed circuit board. **b** The photos of the DC power supply and the impedance analyzer.

Table 1 Electric elements used in experiments.

Electric elements	Company	Packages	Mean value	Tolerance
C_1, C_2	Samsung	0805	1 nF	±5%
L	muRata	1210	39 μH	±5%
R	Panasonic	0603	200 Ω	±1%
OP	Texas instruments	SOIC-8	/	/

$C_{1,2}$, L, R, and OP represent capacitors, inductors, resistors, and operational amplifiers, respectively.

cold atoms, photonic, and phononic metamaterials, to further explore these fascinating phenomena.

Methods

Experimental details. We implement the circuit experiment on a printed circuit broad shown in Fig. 6a. The circuit is composed of 10×11 cells, with each cell containing two nodes. The details of the circuit components are shown in the inset of Fig. 6a. Figure 6b displays the experimental instruments: DC power supply (IT6332A) and impedance analyzer (E4990A), which are used to provide the power for the operational amplifiers and measure the impedance over the sample, respectively.

In Table 1, we list all elements used in our experiments, including the product companies, packages, mean values and their tolerances.

Data availability

Data available upon request from the authors.

Code availability

Code available upon request from the authors.

Received: 19 March 2023; Accepted: 28 July 2023;
Published online: 10 August 2023

References

1. Kogut, J. B. The lattice gauge theory approach to quantum chromodynamics. *Rev. Mod. Phys.* **55**, 775 (1983).
2. Gattringer, C. & Lang, C. B. Quantum Chromodynamics on the Lattice. Lecture Notes in Physics 788 (Springer, 2010).
3. DeTar, C. & Gottlieb, S. Lattice quantum chromodynamics comes of age. *Phys. Today* **57**, 45 (2004).
4. Nielsen, H. B. & Ninomiya, M. A no-go theorem for regularizing chiral fermions. *Phys. Lett. B* **105**, 219 (1981).
5. Chandrasekharan, A. & Wiese, U.-J. An introduction to chiral symmetry on the lattice. *Prog. Part. Nucl. Phys.* **53**, 373 (2004).
6. Ginsparg, P. H. & Wilson, K. G. A remnant of chiral symmetry on the lattice. *Phys. Rev. D* **25**, 2649 (1982).
7. Semenoff, G. W. Condensed-matter simulation of a three-dimensional anomaly. *Phys. Rev. Lett.* **53**, 2449 (1984).
8. Messias de Resende, B., Crasto de Lima, F., Miwa, R. H., Vernek, E. & Ferreira, G. J. Confinement and fermion doubling problem in Dirac-like Hamiltonians. *Phys. Rev. B* **96**, 161113(R) (2017).
9. Yang, Z., Schnyder, A. P., Hu, J. & Chiu, C. Fermion doubling theorems in two-dimensional non-hermitian systems for fermi points and exceptional points. *Phys. Rev. Lett.* **126**, 086401 (2021).
10. Haldane, F. D. M. Model for a quantum Hall effect without Landau Levels: Condensed-matter Realization Of The "Parity Anomaly". *Phys. Rev. Lett.* **61**, 2015 (1988).
11. Yu, Z., Wu, W., Zhao, Y. X. & Yang, S. A. Circumventing the no-go theorem: a single Weyl point without surface Fermi arcs. *Phys. Rev. B* **100**, 041118(R) (2019).
12. Castro Neto, A. H., Guinea, F., Peres, N. M. R., Novoselov, K. S. & Geim, A. K. The electronic properties of graphene. *Rev. Mod. Phys.* **84**, 109 (2009).
13. Qi, X.-L. & Zhang, S.-C. Topological insulators and superconductors. *Rev. Mod. Phys.* **83**, 1057 (2011).
14. Armitage, N. P., Mele, E. J. & Vishwanath, A. Weyl and Dirac semimetals in three-dimensional solids. *Rev. Mod. Phys.* **90**, 015001 (2018).
15. Lv, B. Q., Qian, T. & Ding, H. Experimental perspective on three-dimensional topological semimetals. *Rev. Mod. Phys.* **93**, 025002 (2021).
16. Zhang, W. et al. Observation of flat-band localizations and topological edge states induced by effective strong interactions in electrical circuit networks. *Commun. Phys.* **4**, 250 (2021).
17. Zhou, X., Zhang, W., Sun, H. & Zhang, X. Observation of flat-band localizations and topological edge states induced by effective strong interactions in electrical circuit networks. *Phys. Rev. B* **107**, 035152 (2023).
18. Motavassal, A. & Jafari, S. A. Circuit realization of a tilted Dirac cone: platform for fabrication of curved spacetime geometry on a chip. *Phys. Rev. B* **104**, L241108 (2021).
19. Lu, Y. et al. Probing the Berry curvature and Fermi arcs of a Weyl circuit. *Phys. Rev. B* **99**, 020302(R) (2019).
20. Song, L., Yang, H., Cao, Y. & Yan, P. Square-root higher-order Weyl semimetals. *Nat. Commun.* **13**, 5601 (2022).
21. Jia, N., Clai, O., Ariel, S., David, S. & Jonathan, S. Time- and site-resolved dynamics in a topological circuit. *Phys. Rev. X* **5**, 021031 (2015).
22. Albert, V. V., Glazman, L. I. & Jiang, L. Topological properties of linear circuit lattices. *Phys. Rev. Lett.* **114**, 173902 (2015).
23. Zhao, E. Topological circuits of inductors and capacitors. *Ann. Phys.* **399**, 289 (2018).
24. Imhof, S. et al. Topolectrical-circuit realization of topological corner modes. *Nat. Phys.* **14**, 925 (2018).
25. Lee, C. H. et al. Topolectrical circuits. *Commun. Phys.* **1**, 39 (2018).

26. Hadad, Y., Soric, J. C., Khanikaev, A. B. & Alú, A. Self-induced topological protection in nonlinear circuit arrays. *Nat. Electron.* **1**, 178 (2018).
27. Hofmann, T., Helbig, T., Lee, C. H., Greiter, M. & Thomale, R. Chiral voltage propagation and calibration in a topolectrical Chern circuit. *Phys. Rev. Lett.* **122**, 247702 (2019).
28. Wang, Y., Price, H. M., Zhang, B. & Chong, Y. D. Circuit implementation of a four-dimensional topological insulator. *Nat. Commun.* **11**, 2356 (2020).
29. Helbig, T. et al. Generalized bulk-boundary correspondence in non-Hermitian topolectrical circuits. *Nat. Phys.* **16**, 747 (2020).
30. Chen, R., Chen, C.-Z., Gao, J.-H., Zhou, B. & Xu, D.-H. Higher-order topological insulators in quasicrystals. *Phys. Rev. Lett.* **124**, 036803 (2020).
31. Olekhno, N. A. et al. Topological edge states of interacting photon pairs emulated in a topolectrical circuit. *Nat. Commun.* **11**, 1436 (2020).
32. Song, L., Yang, H., Cao, Y. & Yan, P. Realization of the square-root higher-order topological insulator in electric circuits. *Nano. Lett.* **20**, 7566 (2020).
33. Yang, H., Li, Z.-X., Liu, Y., Cao, Y. & Yan, P. Observation of symmetry-protected zero modes in topolectrical circuits. *Phys. Rev. Res.* **2**, 022028(R) (2020).
34. Zhang, X. X. & Franz, M. Non-Hermitian exceptional Landau quantization in electric circuits. *Phys. Rev. Lett.* **124**, 046401 (2020).
35. Yang, H., Song, L., Cao, Y., Wang, X. R. & Yan, P. Experimental observation of edge-dependent quantum pseudospin Hall effect. *Phys. Rev. B* **104**, 235425 (2021).
36. Yang, H., Song, L., Cao, Y. & Yan, P. Experimental realization of two-dimensional weak topological insulators. *Nano. Lett.* **22**, 3125 (2022).
37. Ventra, M. D., Pershin, Y. V. & Chien, C.-C. Custodial chiral symmetry in a su-schrieffer-heeger electrical circuit with memory. *Phys. Rev. Lett.* **128**, 097701 (2022).
38. Yang, H., Song, L., Cao, Y. & Yan, P. Observation of type-III corner states induced by long-range interactions. *Phys. Rev. B* **106**, 075427 (2022).
39. Wu, J. et al. Non-Abelian gauge fields in circuit systems. *Nat. Electron.* **5**, 635 (2022).
40. Fu, B. et al. Quantum anomalous semimetals. *npj Quantum Materials* **7**, 94 (2022).
41. Dirac, P. A. M. The quantum theory of the electron. *Proc. R. Soc. A* **117**, 610 (1928).
42. Zheng, X., Chen, T. & Zhang, X. Topolectrical circuit realization of quadrupolar surface semimetals. *Phys. Rev. B* **106**, 035308 (2022).
43. Asbóth, J. K. et al. A Short Course on Topological Insulator. Lecture Notes in Physics 919 (Springer, 2016).
44. Yu, H., Xiao, J. & Schultheiss, H. Magnetic texture based magnonics. *Phys. Rep.* **905**, 1 (2021).
45. Chen, S. et al. Recent progress on topological structures in ferroic thin films and heterostructures. *Adv. Mater.* **33**, 2000857 (2021).
46. Tokura, Y. & Kanazawa, N. Magnetic skyrmion materials. *Chem. Rev.* **121**, 2857 (2021).
47. Fert, A., Reyren, N. & Cros, V. Magnetic skyrmions: advances in physics and potential applications. *Nat. Rev. Mater.* **2**, 17031 (2017).
48. Zou, J.-Y. et al. Half-quantized Hall effect and power law decay of edge-current distribution. *Phys. Rev. B* **105**, L201106 (2022).
49. Kim, D.-Y. et al. Quantitative accordance of Dzyaloshinskii-Moriya interaction between domain-wall and spin-wave dynamics. *Phy. Rev. B* **100**, 224419 (2019).
50. Chen, J., Hu, J. & Yu, H. Chiral emission of exchange spin waves by magnetic skyrmions. *ACS Nano* **15**, 4372 (2021).
51. Araki, H., Mizoguchi, T. & Hatsugai, Y. Phase diagram of a disordered higher-order topological insulator: a machine learning study. *Phy. Rev. B* **99**, 085406 (2019).
52. Wakao, H., Yoshida, T., Araki, H., Mizoguchi, T. & Hatsugai, Y. Higher-order topological phases in a spring-mass model on a breathing kagome lattice. *Phys. Rev. B* **101**, 094107 (2020).
53. Schnyder, A. P., Ryu, S., Furusaki, A. & Ludwig, A. W. W. Classification of topological insulators and superconductors in three spatial dimensions. *Phys. Rev. B* **78**, 195125 (2008).

Acknowledgements

This work was supported by the National Key Research Development Program under Contract No. 2022YFA1402802 and the National Natural Science Foundation of China (Grants No. 12074057, No. 11604041, and No. 11704060).

Author contributions

P.Y. and H.Y. conceptualized the project. H.Y. developed the theory and wrote the manuscript supervised by P.Y. and Y.C. H.Y. and L.S. designed the circuits and performed the measurements. All authors discussed the results and revised the manuscript.

Competing interests

The authors declare no competing interests.

Additional information

Supplementary information The online version contains supplementary material available at https://doi.org/10.1038/s42005-023-01326-6.

Correspondence and requests for materials should be addressed to Peng Yan.

Peer review information *Communications Physics* thanks the anonymous reviewers for their contribution to the peer review of this work. A peer review file is available.

Reprints and permission information is available at http://www.nature.com/reprints

Publisher's note Springer Nature remains neutral with regard to jurisdictional claims in published maps and institutional affiliations.

Open Access This article is licensed under a Creative Commons Attribution 4.0 International License, which permits use, sharing, adaptation, distribution and reproduction in any medium or format, as long as you give appropriate credit to the original author(s) and the source, provide a link to the Creative Commons licence, and indicate if changes were made. The images or other third party material in this article are included in the article's Creative Commons licence, unless indicated otherwise in a credit line to the material. If material is not included in the article's Creative Commons licence and your intended use is not permitted by statutory regulation or exceeds the permitted use, you will need to obtain permission directly from the copyright holder. To view a copy of this licence, visit http://creativecommons.org/licenses/by/4.0/.

© The Author(s) 2023